Measurements of parametric instabilities at laser intensities relevant to strong shock generation

G. Cristoforetti[1], L. Antonelli[2], S. Atzeni[2], F. Baffigi[1], F. Barbato[3], D. Batani[4], G. Boutoux[4], A. Colaitis[4], J. Dostal[5,6], R. Dudzak[6,5], L. Juha[6,5], P. Koester[1], A. Marocchino[2,7], D. Mancelli[4,8], Ph. Nicolai[4], O. Renner[6,5], J. J. Santos[4], A. Schiavi[2], M.M. Skoric[9], M. Smid[6], P. Straka[6], L.A. Gizzi[1]

1 *Intense Laser Irradiation Laboratory, INO-CNR, Pisa, Italy*
2 *Dipartimento SBAI, Università di Roma "La Sapienza", Roma, Italy*
3 *Empa Swiss Federal Laboratories for Materials Science and Technology, 8600 Dübendorf, Switzerland*
4 *Université Bordeaux, CNRS, CEA, CELIA, UMR 5107, F-33405 Talence, France*
5 *Institute of Plasma Physics, Czech Academy of Sciences, 182 00 Prague 8, Czech Republic*
6 *Institute of Physics, Czech Academy of Sciences, 182 21 Prague 8, Czech Republic*
7 *Laboratori Nazionali di Frascati, Via E. Fermi 40 00044 Frascati (Rome) Italy*
8 *Donostia International Physics Center (DIPC), 20018 Donostia/San Sebastian, Basque Country, Spain*
9 *National Institutes of Natural Sciences, Tokyo, Japan*

Abstract

Parametric instabilities at laser intensities in the range (2-6)x10^{15} W/cm^2 (438 nm, 250 ps, 100-300 J) have been investigated in planar geometry at the PALS laser facility via calorimetry and spectroscopy. The density scalelength of the plasma was varied by using an auxiliary pulse to form a preplasma before the arrival of the main laser beam and by changing the delay between the two pulses. Experimental data show that Stimulated Brillouin Scattering (SBS) is more relevant than Stimulated Raman Scattering (SRS) in reducing the energy coupling to shock generation. The level of SBS backscatter and laser reflection is found to be in the range between 3% and 15% of the incident laser energy while Backward SRS (BRS) reflectivity ranges between 0.02 and 0.2%, both the values depending on the plasma density gradient. The observation of half harmonics emission constitutes a signature of Two Plasmon Decay (TPD) occurring at a quarter of the critical density. Experimental results suggest that SRS is driven in beam speckles with high local intensity and show that SRS occurs in bursts, particularly at higher laser intensities, due to the presence of kinetic mechanisms saturating the SRS growth into the speckles. Time-resolved measurements show also that BRS is driven in the trailing part of the laser pulse, where density scalelength has increased significantly and has reached the maximum value. Our measurements indicate that hot electrons are predominantly produced by Stimulated Raman Scattering.

Introduction

Shock ignition (SI) is a promising two-step scheme to Inertial Confinement Fusion (ICF), where a strong converging shock wave is launched at the end of the compression phase to ignite the fuel[1-4]. Both the compression of the DT pellet and the igniting shock wave can be produced by a single tailored laser pulse, consisting of a ns long peak at moderate intensities lower than 10^{15} W cm^{-2} followed by a short intense spike (300-500 ps) at intensities between 10^{15} and 10^{16} W cm^{-2}. The SI approach may allow ignition with a low-velocity implosion, reducing the growth of the Rayleigh-Taylor Instability. In addition, SI is robust with respect to non-uniform spike irradiation and shock synchronization, as predicted by hydrodynamic simulations[5,6] and leads to high gain[7], possibly enabling ignition at moderate laser energies, which are already available at LMJ[8] and NIF facilities[9]. In this context, an extensive preparatory study has been carried out also in the framework of the HiPER project and is now aiming at full scale demonstration at one of the above facilities.

The success of the SI concept depends mainly on the coupling of the laser spike with the extended corona surrounding the imploding shell, where an efficient laser absorption, able to generate a strong shock wave (>300 Mbar), is needed. In recent experiments carried out at the OMEGA laser[10,11] in spherical irradiation geometry, at laser intensities relevant for SI (I ~ $6x10^{15}$ W cm^{-2}), a peak ablation pressure close to 400 Mbar was inferred, which constitutes a significant breakthrough towards the demonstration of the feasibility of the SI scheme. Despite this step forward, the physics of laser-plasma interaction in this highly non-linear regime is still largely unknown and needs dedicated investigations. In particular, the growth of parametric instabilities as Stimulated Brillouin Scattering (SBS), Stimulated Raman Scattering (SRS) and Two-Plasmon Decay (TPD), and their interplay, can be considerable and laser filamentation can further enhance their role in the interaction. These processes can significantly degrade laser-plasma coupling due to a strong reflection of light (SBS and SRS) and resulting in the absorption of laser energy in rarefied regions of the corona, far from the ablation layer. Moreover, TPD and SRS generate electron plasma waves that lead to suprathermal electrons via damping. Such electrons, depending on their energy[10-14] may preheat the fuel or affect the shock pressure.

In the last decades, parametric instabilities have been deeply investigated in conditions suitable for direct-drive and indirect-drive schemes[15] of ICF. The majority of these studies, therefore, refer to an interaction regime significantly different from that envisaged for the SI scheme, with laser intensities a factor 10 lower, leaving the interaction regime of interest for SI almost unexplored. The extrapolation of these studies to SI conditions is made complex by the high non linearity of parametric instabilities in this regime. After a rapid boost, instabilities can show a saturation, due to non-linear effects limiting the growth of electron plasma waves (EPW) or ionic acoustic waves (IAW) in the interaction region. EPW decay via Langmuir Decay Instability[16,17] and ponderomotive trapping of thermal electrons in the EPW field are classical examples of phenomena leading to EPW saturation. More recently, other non linear mechanisms, such as bowing and filamentation of EPW into laser speckles[18,19], collective speckle effects[20] or instability cascades have been suggested. All these mechanisms produce a phase detuning of the waves, which in many cases results in consecutive stages of damping and excitation of instabilities, in a burst-like chaotic behavior[21,22]. A fully kinetic approach is therefore needed to model processes as non-local heat transport or Landau damping in the kinetic regime[18,23,24].

Recently, several attempts have been made to model laser-plasma interactions in SI conditions with fully kinetic massively parallel PIC codes. According to Riconda et al.[25] and Klimo et al.[26,27] most of the laser energy is absorbed at densities lower than $n_c/4$ – where n_c is the critical density for the main beam - and the reflectivity due to parametric instabilities, temporally bunched in trains of bursts, can span from the percent level to the 30-50% of the laser energy. Simulations show the importance of kinetics effects, leading to ps- or subps-long bursts of SRS and of SBS, where SRS sometimes occurs in the inflactionary regime, and to non-Maxwellian distributions of electron energies. Simulations also reveal the importance of modelling 2D and 3D effects such as filamentation, laser spraying, cavitation or side-scattered EPW/light. Unfortunately, 2D numerical simulations carried out in the density range 0.01-0.3 n_c are at present limited to a few picoseconds of interaction, which is much shorter than the ignition spike and which is inadequate to model processes having a small growth rate, such as filamentation. While particle in cell of Vlasov-Fokker-Plank are limited to a few picoseconds due to their computation costs, a series of reduced-hydrodynamic models are being under investigation to partially take into account for some effects that might influence the nanosecond plasma evolution, such as the nonlocal electron transport[28], the parameter instability growth and the fast electron generation[29], and the influence of self induced magnetic fields[30].

A few experiments carried out at OMEGA[10,11,31,32] and LULI facilities[33-35] investigated laser plasma interaction at SI intensities. The overall energy scattered by SRS/SBS in these experiments is disparate, in a range going from a few percent up to ~40-50% of the incident energy, strongly dependent on the irradiation geometry and on the laser intensity. SBS back-reflectivity is found to be around 10% in all the experiments, rising to ~20% when side-scattered light is also considered[34]. SRS reflectivity shows a larger range of variability, going from a few percents in planar irradiation experiments[32-34] up to ~36% in spherical geometry[10,31]. SI experiments at the OMEGA laser facility also suggest that SRS is the dominant mechanism of generation of hot electrons, showing a conversion efficiency as high as ~9% of the laser energy in case of spherical irradiation. Further, they suggest that hot electrons can significantly contribute to the shock formation, by increasing the ablation pressure by ~30%[9]. Both the variability of SRS and its effects on the fuel compression call for additional investigation. In particular, the dependence of SRS threshold and saturation on the beam speckles size need further attention.

In this paper we report and discuss experimental data obtained in a series of experiments carried out in a planar geometry at the Prague Asterix Laser System (PALS)[37] at intensities of interest for the Shock Ignition interaction

regime. The overall description of the diagnostics used and an overview of the experimental results obtained, including the measured pressure of the shock wave, is reported elsewhere[38-42]. Here, we focus on the laser plasma interaction and in particular on the Stimulated Raman Scattering and Two Plasmon Decay instabilities. Despite our density scalelength (~100 μm) and the electron temperature (~2 keV) being lower than those envisaged in a real SI scenario, the data reported here provide a comprehensive study of the growth of parametric instabilities at a laser intensity relevant for SI where very little experimental data exists and where, as discussed above, strong non linearities and interplay between different processes are expected to play a dominant role.

Experimental Setup

A basic scheme of the experimental diagnostic arrangement relevant to the results discussed here is shown in Fig.1, while the complete set up is described elsewhere[38].

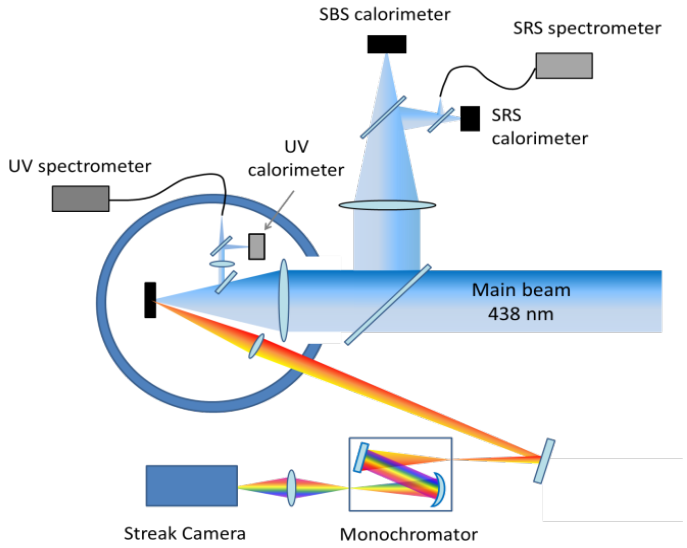

Figure 1: Experimental setup used for parametric instabilities investigation.

The interaction beam, frequency converted to 3rd harmonic (λ_ω = 438 nm) of the fundamental laser frequency and with a duration of 250 ps (FWHM), was smoothed by means of a Random Phase Plate (RPP) and focused at normal incidence on target by an f/2 optical system. The beam profile in the focal spot and the effective energy enclosed in it were accurately measured by imaging and calorimetric techniques. RPP resulted in a Gaussian beam profile of ~100 μm (FWHM) and peak intensity in the range between 2 and $6\text{x}10^{15}$ W cm^{-2}, depending on the energy of the laser shot.

In some shots, an auxiliary beam (not shown in Fig.1) at the fundamental wavelength (λ_0 = 1314 nm, FWHM ≈ 250 ps) and incident at 30° with respect to the target normal, impinged on the target before the main pulse and generated an extended preplasma, mimicking the corona at the end of the compression phase in the shock ignition scheme. The auxiliary beam had a focal spot diameter of ~ 900 μm (FWHM), i.e. much larger than the focal spot of the main beam, to reduce 2D effects during the interaction, resulting in a laser intensity of $\sim 7\text{x}10^{13}$ W cm^{-2}. The delay between the peaks of auxiliary and main pulses was varied in the range between 0 and 1200 ps to change the density scalelength of the preplasma.

Thin multilayer targets were used, consisting of a layer of plastic (C_8H_7Cl, parylene-C) with thickness ranging from 10 to 180 μm on the irradiated side, one or two tracer layers (5 to 10 μm) of Cu and Ti and in some shots a 25 μm-thick Al layer on the rear side. The low-Z material on the front played the role of the ICF ablator material while chlorine ions allowed the plasma temperature to be measured via high-resolution X-ray spectroscopy. Both the spectra and the energy of the light backscattered during the laser plasma interaction were found not to depend on the thickness of the plastic layer nor on the presence of the Al layer. Therefore, these features of the targets are here disregarded. The layers of Cu and Ti were used as markers of hot electrons via K_α photon emission, which was detected by a CCD operating in single-photon regime[43] and by two spherically-bent quartz (422) and (203) crystals imaging spectrometers. Both K_α and X-ray spectrometers used Kodak AA400 films as detectors. A Bremsstrahlung spectrometer using *k*-edge and

differential filtering (14 filters of increasing Z from Al to Pb) was also used with Imaging Plates to measure the x-ray fluence and, indirectly, infer a slope temperature for the hot electron distribution[44]. This spectrometer was looking at front side of the target at ~30° from the laser axis.

The backscattered radiation originating from SRS and SBS/laser reflection was collected by the focusing lens and measured by two calorimeters. On the same line, the radiation was spectrally dispersed by a compact, fiber Vis-IR spectrometer ($\Delta\lambda_{res} \approx 1$ nm), enabling the investigation of backscattered light up to $\omega_0/2$ (λ~876 nm), originating from SRS at densities lower than $n_c/4$ and SRS/TPD instabilities occurring near $n_c/4$. Such spectral resolution, however, did not allow to separate the contribution of SBS and laser reflection in the backreflected emission at λ~438 nm. ~~In addition, l~~Light at $3/2\omega_0$ harmonics of laser frequency (λ~292 nm), originating from TPD, was collected inside the vacuum chamber and sent to a UV spectrometer ($\Delta\lambda_{res} \approx 0.3$ nm) and a calorimeter. Raman scattered light was also collected at a slightly larger angle than the focusing cone (≈20°), spectrally dispersed by a monochromator, and relayed onto the entrance slit of a Hamamatsu C7700 Streak Camera. A spectral range of 100 nm was detected on the camera at a maximum temporal resolution of 8 ps.

Interaction conditions

The interaction conditions of the main pulse, with and without the auxiliary pulse, were modelled via hydrodynamic simulations performed with the codes DUED[45] and CHIC[46]. Fig.2 shows the instantaneous values of temperature and density scalelength $L = n_e/(dn_e/dx)$ at densities $n_c/4$ and $0.12n_c$ for a laser intensity I_{max}= 2.9x10^{15} W cm^{-2} and a delay of 600 ps between auxiliary and main pulses. The $n_c/4$ and $0.12n_c$ densities are the plasma regions were TPD and BRS are driven in the present experiment.

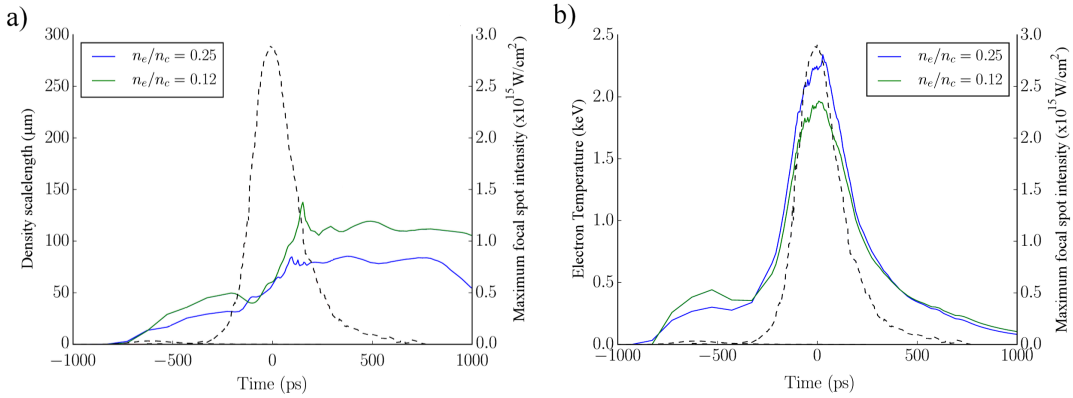

Figure 2: Instantaneous values of density scalelength a) and temperature b) computed at $n_c/4$ and $0.12n_c$ by the CHIC code for a laser intensity I_{max}= 2.9x10^{15} W cm^{-2} and a delay of 600 ps with respect to the auxiliary pulse. The peak intensity of the laser pulse is indicated as a gray line and corresponds to the right-hand side ordinate axis.

Fig.2a shows that the scalelength increases with time, exhibiting a steepening during the main pulse. The values of the scalelength at $n_c/4$ and $n_c/12$ are in the range between 20 and 80 μm and between 40 and 150 μm, respectively, depending on the time and on the delay between the pulses. The scalelength increases with the delay between main and auxiliary pulses, showing a saturation at the longest delays explored. The preplasma scalelength given by the simulations is also in agreement with the 2D plasma density profiles measured by interferometric techniques (*monitor online*)[38] and XRL deflectometry[39].

According to Fig.2b, simulations show a time-dependent temperature, reaching maximum values between 1.4 and 2.5 keV, slightly depending on the laser intensity and density region, in the range of densities 0.10-0.25 n_c. According to the simulations, the temperature of the plasma during the main peak irradiation does not significantly depend on the delay between the pulses, with variations lower than 10%, but is determined by the energy of the main pulse. -Spatially resolved X-ray spectra (not displayed here) , showing well resolved He- and Li-like lines from Cl ions, were compared with SPECT3D predictions[47], providing a temperature averaged over time of ≈700-850 eV for all shots. Such values refer to the overdense region $n_e \approx 3n_c$, for which hydrodynamic simulations predict temperatures of ≈ 800-1000 eV at the time of the main laser peak. A time-averaged value of the temperature of the preformed plasma in the

underdense region was obtained by Cl X-ray spectroscopy, yielding a value of ~175 eV, lower than the peak value of ~300-400 eV obtained by simulations.

Calorimetry

Before presenting SRS and TPD spectra, we briefly depict the extent of parametric instabilities in terms of backscattered energy, obtained by calorimetric measurements, which was already partially presented in Koester et al.[38]. The energy backscattered into the cone of the focusing lens is dominated by light at wavelengths around 438 nm, due to SBS and laser reflection, and ranges between 3% and 15% of the incident laser energy (Fig.3a). On the other hand, SRS gives rise to backreflected light in the spectral range 630-750 nm, consisting of ~0.02% and 0.2 % of laser energy (Fig.3b). Both these values show a clear increasing trend with the prepulse-pump delay, where SBS and SRS reflectivity grows by a factor 2 and 5, respectively, when the delay rises from 0 to 1200 ps. A similar trend is obtained by plotting the intensity of reflected light in the spectral range 600-800 nm, due to SRS (fig.3b). The~~is~~ reasons of this behavior can be~~is~~ ~~easily~~ explained by considering the inhomogeneity of the plasma which determines the convective gain of these instabilities. Regarding the trend in Fig.3a, hydrodynamic simulations show that the amount of backscattered laser light does not increase with the delay between the pulses; therefore we expect that the trend observed is mainly determined by the growth of SBS instability with the delay. Due to the poor spectral resolution, we are unable to determine the plasma density region where SBS is driven. In our interaction conditions, however, the SBS threshold and the convective gain is mainly ruled by the gradient scalelength of the expansion velocity, rather than by the density scalelength[48]. By using the approximate SBS thresholds taken from Kruer[49] and the profiles obtained by hydrosimulations, we find that the SBS threshold in the underdense plasma, which is determined by the velocity gradients, is I_{thres}~(1-2)x10^{15} W/cm^2, while the threshold calculated by considering the density gradient is an order of magnitude lower. Hydrodynamic simulations for shots accounting for a prepulse, however, clearly show that the gradient of the expansion velocity is strongly reduced in the underdense plasma, therefore lowering the SBS threshold and correspondingly boosting the instability gain. This can possibly explain the experimental results plotted in Fig.3a.

Fig.3b, on the other hand, can be easily explained by considering that larger delays produce longer plasmas, resulting in larger gain for the ~~instabilities~~SRS, whose threshold is strongly affected by density scalelength in the plasma. In order to better clarify the relation between the prepulse-pulse delay and the plasma gradient, the values of density scalelength calculated by the code DUED in proximity of the laser peak (I_{max} ≈ 5x10^{15} W cm^{-2}) and at a density $n_e = 0.12\ n_c$ are reported in Fig.3b for fixed values of the delay.

-Calorimetric measurements of $3/2\omega_0$ and $\omega_r/2$ emission, obtained by using an approximate isotropic distribution, give a conversion efficiency $\eta_{3/2}$ around 0.5 % of incident energy and a corresponding value $\eta_{1/2}$ in the range (0.4-2)x10^{-2} %, i.e. a negligible loss of laser energy. Since the actual angular dependence is not known, such values have to be considered only as an order of magnitude.

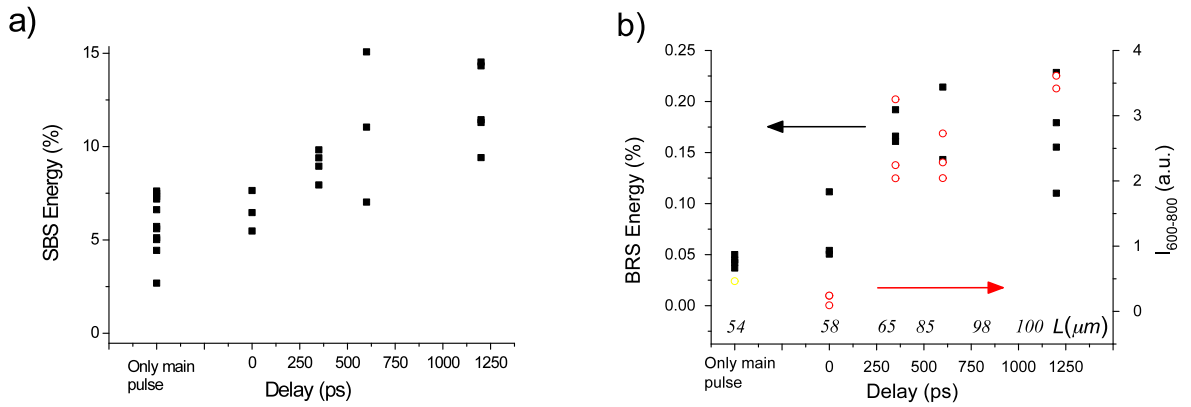

Figure 3: a) Energy backscattered by SBS and laser backscatter (λ=438 nm); b) SRS energy (black squares) and spectral intensity $I_{600\text{-}800}$ integrated in the range 600-800 nm (red circles), versus the delay prepulse-pulse for I_{max} ≈ (3.5-6)x10^{15} W cm^{-2}. Values of

density scalelength calculated by the code DUED in proximity of the laser peak (I_{max}≈ 5x10^{15} W cm^{-2}) and at a density n_e = *0.12* n_c are also reported for fixed values of prepulse-pulse delay.

Half-integer harmonics of laser frequency

Typical $\omega_0/2$ (λ = 876 nm) and $3/2\omega_0$ (λ = 292 nm) spectra are shown in Fig.4. Both spectra exhibit an energy splitting around the harmonic wavelength, which is related to the frequency difference of plasma waves produced by TPD instability at $n_e=n_c/4$.

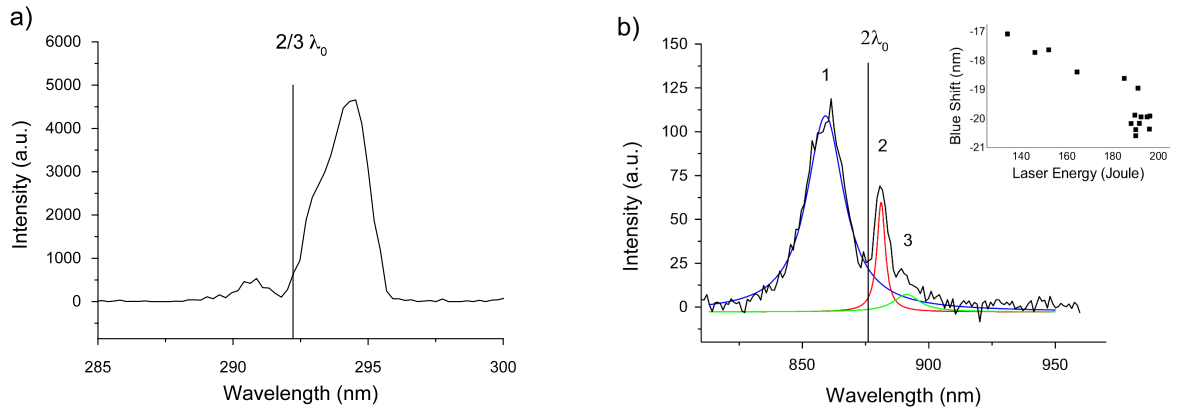

Figure 4: Typical 3/2 ω_0 and $\omega_0/2$ spectra, obtained at I_{max}≈ 5x10^{15} W cm^{-2} (black lines). Vertical lines indicate the position of the nominal laser harmonics. Red, green and blue lines in b) show the peaks resulting by fitting the spectrum using 3 Lorentzian peaks. The inset in b) is a plot of the shift of the blue peak 1 vs. the energy of the laser pulse. Adapted with permission from [65], Copyright 2017 EPL Association.

The frequency shift of TPD blue and red EPWs from the central frequency $\omega_0/2$ can be expressed by

$$|\delta\omega|/\omega_0 = \frac{9}{4}\left(v_{th}^2/c^2\right)\kappa \qquad (1)$$

where $\kappa = \mathbf{k_B}\cdot\mathbf{k_0}/k_0^2 - 1/2$, k_B is the blue EPW wave-vector and v_{the} is the thermal velocity[5048].

The well-defined structure of $\omega_0/2$ (Fig.4b) agrees with the relevant literature on the topic[5149,5220]. Beside the evident blue- and red-shifted peaks (labelled 1 and 2, respectively), a less evident bump at longer wavelengths (peak 3) is visible, which we identify as a supplementary peak, as in Seka et al.[5149]. The blue peak has a shift from the nominal $2\lambda_0$ wavelength and a width significantly larger than the red peak 2, approximately 3 and 3.6 times, respectively. Conversely, the shift of peak 1 is similar to the shift of the weak peak 3. The different frequency shift of peaks 1 and 3 ($\overline{\Delta\omega_{1,3}}/\omega_0$ = 1.1x10^{-2}) and peak 2 ($\overline{\Delta\omega_2}/\omega_0$ = 3.4x10^{-3}) indicates that the EPWs responsible for them have different wave-vectors and a different origin. This is possible since TPD instability in an inhomogeneous plasma can generate different EPWs in the range allowed by the Landau damping.

Both the frequency shifts increase with laser energy, as visible in the inset of Fig.4b for the blue peak. In previous works[5149], the sharp peak 2 was observed at laser intensities higher than TPD threshold but much lower than SRS threshold. For this reason, this is usually associated to a hybrid TPD/SRS instability rather than to a pure absolute SRS instability, where a pump electromagnetic wave decays in a forward electrostatic wave with $k\approx k_0$ (as TPD and SRS) and in a backward partly electrostatic and partly electromagnetic wave[5341] in the proximity of the $n_c/4$ surface (here $n_e/n_c \approx 0.24$). According to Seka et al.[5149], the shift of this peak in $\omega_0/2$ spectrum, differently from $3/2\omega_0$ splitting,

is well applicable for the estimation of the plasma temperature because it is not affected by the angle of observation or by geometrical effects, such as filamentation, cavitation or 2D profiles. By using Eq.(1) with $\kappa = ½$, we obtain a plasma temperature which increases from 1.35 keV to 1.68 keV when I_{max} rises from 2.4×10^{15} to 3.7×10^{15} W cm^{-2}. This value agrees with plasma temperature given by simulations, considering that it is calculated from time-integrated measurements; moreover, as shown below, it agrees with the Landau cutoff of Raman spectrum produced at densities $n_e < n_c/4$.

According to literature[52], the broad peak 1 and the small peak 3 can be generated by Inverse Resonance Absorption (IRA) or by Raman Downscattering (RD) of a laser photon. In the IRA process, a EPW with $k/k_0 < 0.1$ is converted into a photon near its turning point; therefore blue and red peaks are originated by conversion of blue and red EPWs, respectively. In the RD process, conversely, a laser photon is down-scattered by a EPW produced by TPD, so that blue and red peaks are generated by scattering with red and blue EPWs, respectively. Both IRA and RD need particular matching conditions[51~~49~~,54~~2~~], and many authors have speculated on the prevalence of the one or the other in different experiments. Here, both coupling conditions can be fulfilled near $n_c/4$, where filamentation, turbulence, cavitation and laser photon scattering can occur. For these reasons, it is here not possible to definitively exclude neither IRA nor RD. We note however that a blue shift $\Delta\lambda_B \approx 20$ nm implies $\kappa \approx$ ~~2~~1.7, indicating the involvement of EPWs with wave-vector $k_e \approx 2.$~~9~~$k_0$3k_0. By taking a plasma temperature $T_e \approx 1.5$ keV, as estimated above, we obtain $k_e\lambda_D \approx 0.27$, indicating that EPWs originating the broad peaks 1 and 3 are located near the Landau cutoff at densities $n_e/n_c \approx 0.21 - 0.22$. According to linear theory[55], TPD driven in such low density region is expected to occur in convective regime, as previously found both in experiments and numerical calculations[51,56,57]. Such modes could be generated by ion density fluctuations driven by the ponderomotive force of the EPWs driven at $n_c/4$, which successively propagate down to lower densities[58]. By using 2D PIC simulations with ISIRIS code, Yan et al. showed that after a linear growth stage, such modes could be coupled with the SRS/TPD mode near the $n_c/4$ surface via plasma waves and pump-depletion, giving rise to an intermittent bursting pattern of the instability[21].

Three-halves harmonic peaks are due to the coupling of laser photons with TPD EPWs. The blue peak is much weaker than the red one, which can be ~~is usually~~ explained by the fact that the blue EPW must be reflected at its critical density in order that the $3/2\omega_0$ blue peak is observed in the backscattering direction[51]. Otherwise, the blue peak can be generated by the EPW resulting from the Langmuir Decay Instability of the primary TPD wave, as shown by Russel et al.[59].The frequency shift of blue and red peaks is $\overline{\Delta\omega_{3/2}}/\omega_0 \approx 1.09 \times 10^{-2}$, i.e. similar to that of peaks 1 and 3 of $\omega/2$ spectrum, suggesting that EPWs responsible for these harmonics are the same, located near the Landau cutoff.

The splitting of half harmonic spectra show that TPD (including hybrid TPD/SRS instability) dominates on absolute SRS at the quarter critical density. This is in qualitative agreement with 2D PIC simulations by Weber et al.[60~~53~~], performed with values of temperature and density scalelength similar to our experiment. Simulations referring to hotter plasmas in SI conditions[26,27] indicate instead a large contribution of absolute SRS at $n_c/4$.

Backward Stimulated Raman Scattering

The SRS instability driven at densities lower than $n_c/4$ gives rise to light scattered in the spectral range $\omega_0/2 < \omega < \omega_0$. All the measured emission spectra exhibit peaks in the 630-750 nm spectral range, as shown in the time resolved spectrum in Fig.5, obtained with laser intensity $I_{max} \approx 3.4 \times 10^{15}$ W cm^{-2} and no auxiliary pulse. The same figure reports also a typical spectrum lineout and the temporal profiles of the emission compared to the laser pulse (discussed below). The emission has a complex and not reproducible spectral structure, with an overall bandwidth usually increasing with the delay between auxiliary and main pulses (Fig.6a). The intensity of this emission grows with laser energy, for a fixed delay, showing a saturation fort $\Delta t = 1200$ ps (Fig.6b).

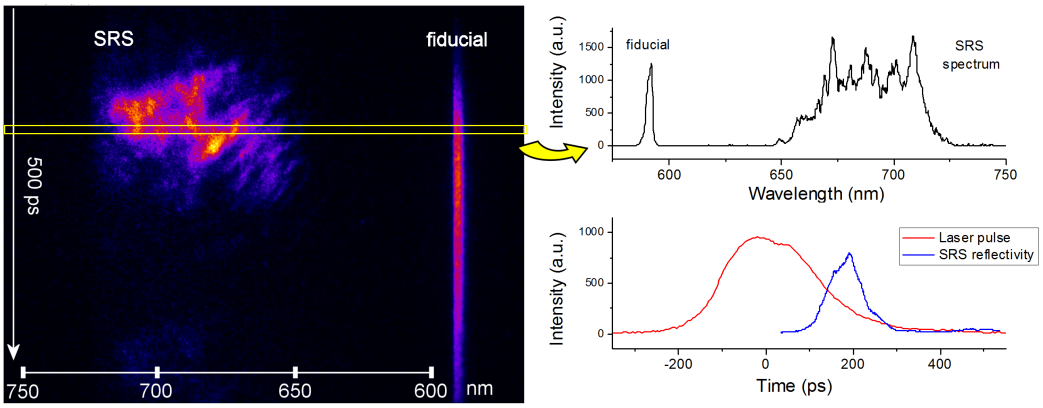

Figure 5: on the left, time-resolved SRS spectrum obtained with laser intensity $I_{max} \approx 3.4 \times 10^{15}$ W cm^{-2} and no auxiliary pulse. The acquisition time window, spanning in the vertical axis, is 500 ps. On the right top is reported the SRS spectrum emitted in the selected time window of Δt=20 ps, as shown on the left. On the right bottom, the temporal profiles of laser pulse and SRS emission are shown.

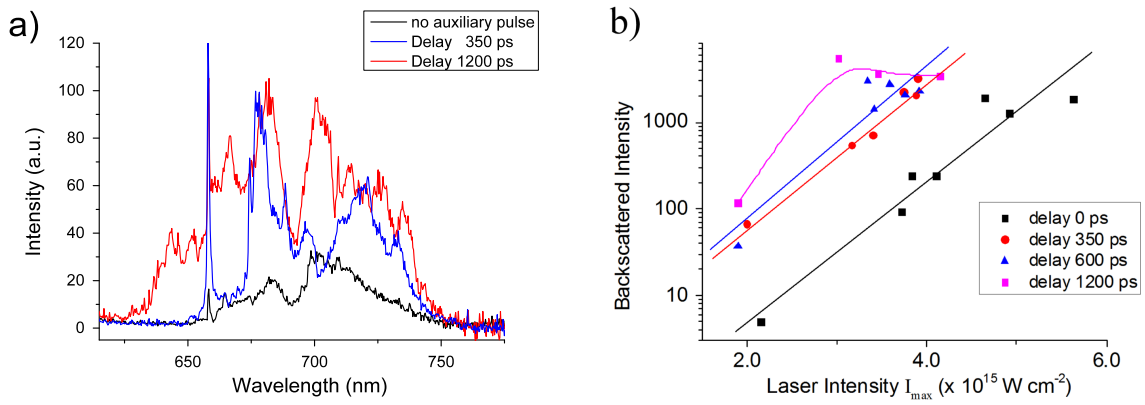

Fig.6: a) SRS spectra obtained with laser intensity $I_{max} \approx (3.5\text{-}5.5) \times 10^{15}$ W cm^{-2} and delays between prepulse and pump pulse of 350 and 1200 ps, are compared with the spectrum obtained without the auxiliary pulse. b) curves of growth of SRS intensity for different values of the delay prepulse-pump are shown.

We associate these peaks to Backward Stimulated Raman Scattering (BRS) occurring in the underdense plasma. Matching conditions and a plasma temperature of ~1.5 keV, taken as an effective value during the laser peak, imply that BRS is excited in the density range 0.10-0.15 n_c and drives forwardly directed EPWs with wave-vector k_e= 1.37-1.52 ω_0/c. The lower wavelength cutoff of the emission (n_e/n_c = 0.10) corresponds to a value of $k_e\lambda_D \approx 0.28$ ~~28~~ 27 which agrees with a cutoff due to Landau damping of plasma waves; this value, indirectly, confirms the value of the plasma temperature in the underdense plasma estimated above.

a) SRS threshold and role of speckles

Stimulated Raman Scattering is driven by local values of the laser intensity. An investigation of SRS threshold in the present experiment therefore must account for the distribution of e.m. fields in the micro-scale. The use of a Random Phase Plate on the laser beam results in the reduction of longitudinal and transverse spatial coherence length[61~~54~~] yielding small speckles of size $l_\perp \approx 2F\lambda_0$=1.6 μm and length $l_\parallel \approx 8F^2\lambda_0$ ~14 μm (F is the f-number of the system). Taking into account the expected laser intensity distribution in the speckles and the number of speckles expected in the focal volume (≈ 10^5), maximum local laser intensity should reach ~8-10 I_{max}. Speckle dimensions and intensity distribution control both filamentation and parametric instabilities occurring during the interaction. Here,

ponderomotive self focussing of most intense speckles (I > (2-3)x10^{16} W/cm^2) is expected to occur at densities relevant for SRS and TPD processes, while for lower intensity speckles filamentation is inhibited by their small dimensions.

The threshold of SRS instability in speckles depends on many factors, including their possible filamentation and collective effects between speckles. The issue becomes much more complex in the kinetic regime ($k_e\lambda_D$>0.2), where non-linear Landau damping effect, depending on the electron trapping in EPW and on their side loss across filaments, plays an important role. Here, BRS threshold is basically estimated by considering the main damping effects of electron plasma waves. In inhomogeneous density profiles, the main source of damping is usually the limited resonance region where matching conditions are satisfied. The length l of this region is set by imposing $\int_o^l \kappa dx \approx 1/2$, where $\kappa = k_0 - k_s - k_e$ is the wavenumber mismatch of the interacting waves. Here, assuming a linear density profile in the resonant region, we calculate l ~1.5 μm ≈ 3.4 λ_0 resulting in an effective damping rate of $v_s/l = 4\cdot10^{-2}\omega_0$ ~~s^{-1}~~ for the scattered e.m. wave and of $v_e/l = 1.53\cdot10^{-3}\omega_0$ ~~s^{-1}~~ for the EPW, where v_s and v_e are the group velocities of the two waves.

Relying on classical theory, the growth of convective SRS can be expressed by $I_{SRS} = I_{noise}\exp(2\pi\lambda)$ with the Rosenbluth parameter $\lambda = \gamma_0^2/\kappa'|v_e v_s| = (\gamma_0 l/v_s)(\gamma_0 l/v_e)$, where γ_0 is the homogenous growth rate, and the two terms in brackets correspond to the number of e-folds in length l of scattered e.m. wave and of EPW, respectively[62~~55~~]. It is useful to plot the value of spectrally integrated intensity I_{SRS} versus the product $I{\cdot}L$ where laser intensity I is proportional to γ_0^2 and density scalelength L is proportional to $1/\kappa'$ (see e.g. Liu et al.[63~~56~~]). Given the time and space dependence of laser intensity, we here considered the intensity I_{av} averaged over one standard deviation in time and space (I_{av}=I_{max}/1.366). Density scalelength values L were taken from the DUED and CHIC hydrodynamic simulations for the different shot conditions (intensity, delay).

We observe that this representation – shown in the plot of Fig.7 – strongly reduces the scatter of points as compared to what obtained in the graph of I_{SRS} vs. I (Fig.6b) and therefore seems to effectively account for both the effects of laser intensity and density scalelength; besides, the approaching of points supports the hypothesis that the Rosenbluth parameter, via the product $I{\cdot}L$, is the parameter determining the SRS threshold and growth in our experiment. Fig.7 also shows that the BRS emission rapidly grows for smaller $I_{av}{\cdot}L$ values and tends to saturate at larger values.

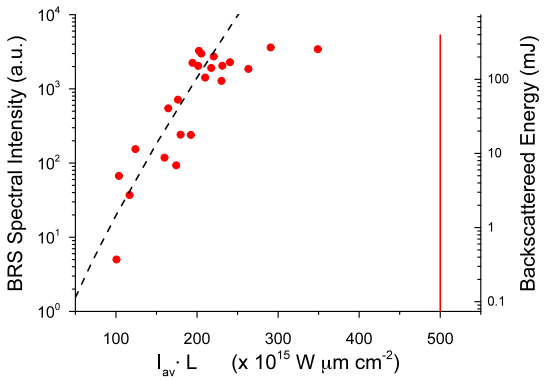

Figure 7: BRS intensity versus the product $I_{av}{\cdot}L$ appearing in the Rosenbluth parameter, where I_{av} is the laser intensity averaged over one standard deviation in time and space. The dashed line represents the rate of BRS expected from Rosenbluth theory, calculated for single pulse irradiation.

According to Liu et al.[63~~56~~], the threshold for BRS in inhomogeneous plasmas, obtained by considering wavenumber mismatch conditions, can be calculated by

~~$v_0^2/c^2 > 1/k_0 L$ (2),~~

where v_0 is the quiver velocity of an electron in the e.m. laser field. The threshold ~~given by Eq.(2)~~ is therefore I^{BRS} = (4.5-8)x10^{15} W cm^{-2} depending on the prepulse-main pulse delay~~. A similar value can be obtained by using~~

~~expressions reported by Liu et al.[56]~~. It is worth noting that in Fig.7, the threshold is represented by the red vertical line $I_{thres} \cdot L$ = 500x10^{15} W μm cm^{-2}, showing that SRS threshold is above the laser intensity in all our shots. Such value can be inaccurate for several reasons, among them the effect of Landau damping to be considered in kinetic regime, the damping due to the side-loss of electrons across the speckle edge and the possible flattening of density profile due to filamentation of speckles, which ~~both~~ all need 3D fully kinetic simulations to be correctly estimated. The calculated threshold, however, suggests that local intensity in speckles, higher than the envelope laser intensity, is needed to drive BRS. At the lowest laser intensities, only speckles with intensities 5 times higher than I_{av} can drive BRS. Conversely, at higher laser intensities, also speckles with local intensity marginally higher than I_{av} can play a role.

This picture is even reinforced by accounting for other EPW damping processes, beyond the escape of the EPW from the resonance region. Considering the present interaction conditions (T_e=1.5 keV, λ_{SRS}=680 nm, speckle size $l_\perp \approx 1.6$ μm), Landau and side-loss[64] damping rates are $\gamma_L \approx 9 \cdot 10^{-4} \omega_0$ and $\gamma_{SL} \approx 2 v_{th}/l_\perp = 1.5 \cdot 10^{-3} \omega_0$, while collisional damping ν_{ei} is an order of magnitude lower. It is therefore evident that Landau damping of EPWs is not expected to affect seriously the saturation of SRS, while the side loss of electrons, due to the low f/# number of focusing optics, is more effective in limiting the convective gain. ~~correcting the BRS threshold for Landau damping of EPWs with a classical approach. Considering backscattered emission λ_{SRS}=680 nm and T_e=1.5 keV, Landau damping of EPWs is γ_L ~~ 4.5x10^{12} ~~s^{-1} (collisional damping ν_{ei} is an order of magnitude lower).~~ Accounting for both convection out of resonance region and ~~Landau~~ side loss damping of EPWs, BRS threshold shifts to values near $I_{thres} \cdot L$ = ~~800x10^{15}~~-950x10^{15} (with a slight dependence on L), which implies an even stronger role of high intensity speckles. A more accurate investigation of the effect of high intensity speckles on the BRS amplification in the present data can be found in Cristoforetti et al.[65~~58~~], where the experimental results are compared to those obtained by the radiative- hydrodynamic code CHIC. In addition to laser refraction and diffraction, the code also accounted for the laser intensity statistics contained in the beam speckles and included self-consistent calculations of non-linear laser plasma interactions[29]. The results of the simulations clearly show that a correct modeling of the speckle intensity statistics into the beam allows reproducing the SRS reflectivity experimentally observed.

b) Saturation and kinetic effects

Figs.6b and Fig.7 show a rapid BRS growth and a saturation at higher intensities and scalelengths, visible in particular at delays of 600 and 1200 ps. SRS growth with $I_{av} \cdot L$ is expected to be a combined effect of the larger intensity in single speckles, and of the increasing number of speckles overcoming I_{thres}. The comparison of the experimental SRS intensities with the SRS growth predicted by the classical Rosenbluth growth rate[62~~55~~], shown in Fig.7, reveals that the convective theory well reproduces the experiment for $I_{av} \cdot L$ < 240x10^{15} W μm cm^{-2}, i.e. before that the SRS saturation becomes evident. The expected SRS growth rate, displayed by the dashed line in Fig.7, is obtained by considering single pulse irradiation and supposing that SRS signal observed at $I_{av} \cdot L$ = 100x10^{15} W μm cm^{-2} is originated by speckles immediately after the threshold. The gain is here not calculated from thermal noise, but just fitting the points at lower intensities. It is worth to remark that the predicted curve does not include the fact that an increasing number of speckles contributes to BRS intensity for larger values of I_{av}, which would make the curve steeper than that plotted in the graph, increasing the discrepancy with experimental results in particular in the saturation region. The SRS saturation observed at the highest $I_{av} \cdot L$ values suggests that damping and kinetic effects lead to saturation of SRS into the speckles.

A similar growth rate, by 1-2 orders of magnitude in scattered light level in less than a factor 2 increase of laser intensity, followed by a rapid saturation has also been found in experiments carried out at Trident laser facility[16] aimed at investigating SRS occurring in single hot spots, as well as in PIC simulations in kinetic regime reported in literature[18,66-68~~59,60~~]. In these works, the saturation is due to a nonlinear frequency detuning occurring in large EPWs excited in the BRS process[69~~3~~,70~~64~~]. The frequency shift can be due to ponderomotive and electron trapping effects as for example in bowing and filamentation of plasma waves in speckles[18,66~~59~~]. It was found[22,67,68,71~~60~~,7-62, ~~2~~] that the nonlinear phase detuning results also in a non-stationary Raman saturation, in the form of a transition from a strongly modulated quasi-periodic to intermittent chaotic regime, with an increasing laser intensity[22,73~~65~~]. Since the SRS saturation is not mainly determined by Landau damping, but rather by convective and side loss effects, we don't expect that inflactionary SRS or autoresonance[74] effects due to the ponderomotive trapping of electrons were relevant for SRS growth, as discussed by Vu et al.[64]

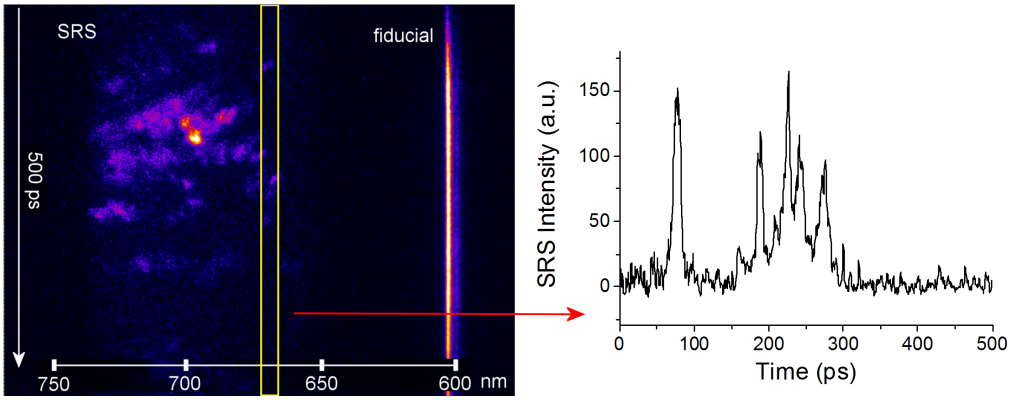

Figure 8: on the left, time-resolved SRS spectrum in the saturation region (I_{av}·L = 280x10^{15} W μm cm^{-2}) obtained with laser intensity $I_{max} \approx 4.5 \cdot 10^{15}$ W cm^{-2} and no auxiliary pulse is shown. The acquisition time window, spanning in the vertical axis, is 500 ps, and the time resolution is ≈8 ps . On the right the time profile of SRS emission in the spectral range λ = 670 ± 3 nm.

The occurrence of kinetics mechanisms in BRS saturation in the present experiment is suggested by the chaotic character of spectra in Fig.6a. Intensity dependent incoherent spectral broadening could be, in fact, attributed to nonlinear saturation of BRS with large bursts and quasi-periodic pulsations in intensity, as observed in kinetic simulations[7611,7622]. According to theory and PIC simulations, kinetic mechanisms are expected to result in non-stationary SRS saturation and reflectivity bursts of the duration of the order of the ps or lower[20,7622,7365]. Time-resolved BRS spectra in the saturation region (I_{av}·L > 240x10^{15} W μm cm^{-2}) with high temporal resolution (Δt ≈8 ps), show evidence of emission bursts, as shown in Fig.8. The temporal lineout of streak images reveals that the typical time duration of emission bursts is FWHM ≈8-10 ps, i.e. limited by the time resolution of the streak-camera. This is consistent with numerical PIC results and constitutes a confirmation of the presence of kinetic mechanisms in the SRS saturation regime.

c) Timing of SRS emission

The temporal evolution of SRS reflectivity exhibits a bursty behavior, as pointed out above, and a considerable delay with respect to the peak of the laser pulse, as shown in Fig.5. The delay between BRS and laser peaks, measured only in the case of shots without the auxiliary pulse, was ~190-220 ps. The reflectivity due to Stimulated Raman Scattering is observed at even longer times, up to 300 ps after the laser peak, when laser intensity is very low. In order to understand this trend, hydrodynamic simulations with the radiative-hydrodynamic code CHIC were carried out. As in Cristoforetti et al.[6558], simulations included self-consistent calculations of Stimulated Raman Scattering and generation of hot electrons by appropriate scaling laws using the local and instantaneous values of laser intensity and plasma parameters. The laser temporal profile measured shot by shot in the PALS control room was used in the simulations.

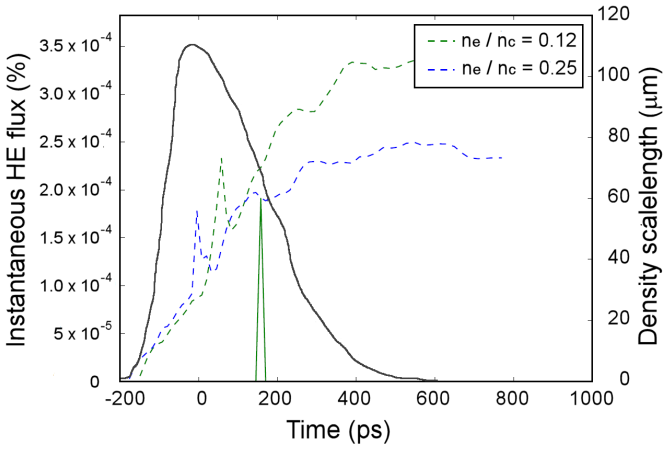

Figure 9: Simulation results for $I_{max} \approx 3.7 \times 10^{15}$ W cm^{-2} and no auxiliary pulse: instantaneous hot electron flux driven by BRS as a function of time (green), density scale lengths computed at $n_c/4$ and 0.12 n_c (dashed blue and green lines, respectively). The peak intensity of the laser pulse is indicated as a gray line.

Simulation results obtained for $I_{max} \approx 3.7 \times 10^{15}$ W cm^{-2} and no auxiliary pulse are shown in Fig.9. Differently from our previous work, here the code was not optimized to reproduce the speckles with highest laser intensity. For this reason, local laser intensity barely overcomes the SRS threshold in a few regions of the laser spot, which explains the low value of the hot electron flux obtained. Consistently with our experimental findings, simulations show that SRS is driven in the trailing part of the laser pulse, here at a time ~~–~~180 ps. Such value is easily understood by looking at the temporal growth of the density scalelength in the plasma, which progressively increases during the laser pulse and reaches the maximum value when the laser pulse is over. Moreover, as shown in Fig.2b, the plasma temperature significantly decreases in the trailing part of the pulse, resulting in a considerable reduction of Landau and side loss damping rates, and then in a corresponding lowering of the SRS threshold. ~~In this way~~These facts explain why~~,~~ the optimal conditions for SRS onset occurs in the tail of the laser pulse.

Hot electrons

Suprathermal electrons propagating into the target give rise to Cu K_α and Ti K_α emission when they cross Cu and Ti tracer layers. X-ray spectroscopy of Cu K_α and Ti K_α emission is therefore here used as a diagnostics of hot electrons. The flux and average energy of HEs were here estimated by measuring the reduction of the Cu K_α and Ti K_α signals when the thickness of plastic layer was increased. By considering the electron stopping range in the different layers (tabulated in ESTAR database of NIST[75~~68~~]), this value allowed to calculate the penetration depth of hot electrons and hence their average energy. Monte Carlo simulations performed with the GEANT4[76~~66~~] and PENELOPE[77~~67~~] codes were used to reproduce the experimental results. Assuming an exponential distribution for hot electron energy ~exp(-E/T_{hot}), a temperature T_{hot}= ~~25~~–20 ± 10 keV and an energy HE conversion ε_{HE} ~ 0.14% ± 0.03% were~~as~~ obtained. Such distribution well fitted the K_α signal obtained for all shots with the exception of those using plastic layers of 125 μm and overall 180 μm. In these shots, the measured K_α emission was higher than expected. This suggests that energetic HEs, with a temperature T_{hot} > 100 keV, are also generated during the interaction. Another approach for estimating hot electron energy is considering the ratio between Cu K_α and Ti K_α emission on the same shot. This value does not depend on the absolute number of generated hot electron, which may vary shot by shot, making this diagnostics more accurate. The HE temperature obtained with this method was T_{hot}= 25 ± 5 keV and the energy conversion ε_{HE} ~ 0.1% ± 0.05% of the incident laser energy. Hot electron energy was also measured by using a bremsstrahlung cannon, resulting in a temperature T_{hot}= 19 ± 3 keV, in agreement with the previous~~previous~~ values referring to the colder temperature.

The measured temperature of ~20 keV is close to that obtained for hot electrons generated by BRS ($T_{hot} \approx 28$ keV), in the 1D PIC simulations of Klimo et al.[26]. Although the simulation time (≈80 ps) is shorter than our laser pulse, the explored range of intensity (2.4-24 PW/cm^2) and the preplasma scalelength (150 μm) are similar to those of the present experiment. In these simulations, however, SRS occurs at densities closer to the quarter critical density, which determines the phase velocity of plasma waves induced by Raman and thus the energy of the hot electrons. Conversely, those simulations turn out in a prevailing component of hot electrons with a lower energy ≈ 10 keV, which are accelerated in cavities seeded at quarter-critical density by SRS and TPD. In the present work, this low-energy hot electron component ~~seems negligible~~is not observed.

The Cu K_α intensities measured by a CCD working in single-photon regime suggest a correlation between the BRS backscattered intensity and the K_α photon number, as shown in Figure 10. This supports a scenario in which hot electrons are mainly generated by breaking of EPW induced by BRS, as in Klimo simulations.

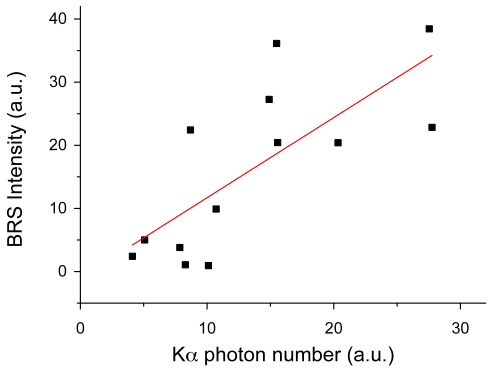

Figure 10: Correlation between BRS intensity and Cu K_α photon number measured with the CCD working in the single photon regime. Reproduced with permission from [65], Copyright 2017 EPL Association.

The energy of the electrons generated by BRS in the density region 0.10-0.15 n_c, obtained by considering the phase velocity $v_{ph} = \omega_e/k_e$ of the driven EPW, is ≈ 17-20 keV, that is in good agreement with the measured value. ~~The measured hot electron energy is in agreement with that predicted by BRS.~~ This again supports the conclusion that such hot electrons, that are the main component, are ~~predominantly~~ produced by BRS~~, and only marginally by TPD~~.

Supposing that the $\omega_0/2$ spectra loosely reflect the frequencies of TPD EPWs, hot electrons of different energy could be generated by the convective modes near the Landau damping and by the hybrid SRS/TPD modes near the $n_c/4$ surface. EPWs in low density regions ($n_e/n_c \approx 0.21-0.22$) are expected to easily trap thermal electrons due to their low phase velocity ($v_{ph} \approx 4v_{th}$), resulting however in low-energy hot electrons ($T_e \approx 10$ keV). A Maxwellian component in the electron distribution at this low temperature was however not clearly observed in our measurements. High frequency hybrid modes, on the other hand, could in principle generate much hotter electrons ($T_e > 100$ keV), but their flux is expected to be limited by the small number of thermal electrons that can be trapped at so large EPW phase velocities ($v_{ph} \approx 10.5v_{th}$). By means of 2D PIC and fluid simulations, Yan et al.[58] recently showed that the amount of these high-energy hot electrons can be significantly enhanced by a staged acceleration of electrons from the low density region ($n_e/n_c \approx 0.21-0.22$), generated by convective modes, to the high density region ($n_e/n_c \approx 0.24-0.25$) where hybrid SRS/TPD modes operate. Such high-energy electrons, that could be deleterious in SI for the possible pre-heating of the compressed fuel, could explain the K_α signal measured for target with large plastic thickness (125 and 180 μm). Since the electrons generated by hybrid SRS/TPD modes are expected to be energetic and strongly peaked in the forward direction, also the generated Bremsstrahlung emission is expected to be mainly emitted in the forward direction[78]. This could explain why their contribution was not detected by the Bremsstrahlung spectrometer, which was located on the irradiated side of the target.

~~while the energy of hot electrons obtained by EPW driven by TPD is expected to be higher, in the range 60-100 keV[26]. The measured hot electron energy is in agreement with that predicted by BRS. This again supports the conclusion that hot electrons are predominantly produced by BRS, and only marginally by TPD.~~

Conclusions

The impact of parametric instabilities at laser intensities relevant for shock ignition in a planar irradiation geometry has been investigated with both calorimetry and spectroscopy. Measurements show that the main mechanism reducing the pulse energy transfer to the plasma is Stimulated Brillouin Scattering and laser backscatter, with reflectivities in the lens cone of 3-15% of laser energy, while the energy backreflected by Stimulated Raman Scattering is lower than 1%. Both $3/2\omega_0$ and $\omega_0/2$ harmonics are well visible in the spectra, a signature that a fraction of laser energy reaches the $n_c/4$ surface and drives TPD and hybrid TPD/SRS instabilities.

Stimulated Raman Scattering is driven at densities compatible with classical Landau cutoff (n_e=0.10-0.15 n_c) in the trailing part of the laser pulse, where the scalelength of the plasma is larger. It results in the generation of a low flux

(~0.1%) of low-energy (T_{hot} ~ 20 keV) hot electrons. Measurements also suggest the presence of a component of high energy hot electrons (T_{hot} > 100 keV), that could be possibly generated by the hybrid TPD/SRS instability. BRS is here driven in the small beam speckles generated by the RPP, where local intensity is much higher than the envelope value. The BRS gain, its spectral modulations and the observation of reflectivity bursts suggest the occurrence of nonlinear and kinetic effects into the speckles, affecting EPW growth and resulting in the Raman saturation. BRS extent is much lower than that measured in other experiments relevant for SI[10,31,33,34], which is partly explainable by the lower plasma scalelength.

Acknowledgments

We would like to thank Prof. S. Hueller for the fruitful discussions and valuable suggestions on the interpretation of Stimulated Raman Scattering data. We would like to acknowledge financial support from the LASERLAB-EUROPE Access to Research Infrastructure activity within the EC's seventh Framework Program (grant agreement no 284464). We also acknowledge the support of Eurofusion project AWP17-ENR-IFE-CEA-01. We acknowledge SciTech Precision and Rutherford Appleton Laboratory Target Fabrication Group for the supplied targets. Finally, we thank the technical staff of PALS for help in running the experiments. We acknowledge financial contribution from the MIUR funded PRIN Project N.2012AY5LEL. Participation of O.R. and M.S. in this research was partly supported by the ELI project CZ.02.1.01/0.0/0.0/15_008/0000162 and High Field Initiative CZ.02.1.01/0.0/0.0/15_003/0000449. Participation of F.B. to this research is supported by the CNR funded Italian research Network ELI-Italy. Participation of S.Atzeni in this research is supported to the project Sapienza 2016 n. 257584. The PALS staff appreciates a financial support from the Czech Ministry of Education (LM2015083 and EF16_013/0001552) and Czech Science Foundation (17-05076S).

References

1 R. Betti, C. D. Zhou, K. S. Anderson, L. J. Perkins, W. Theobald, A. A. Solodov, Phys. Rev. Lett. 98, 155001 (2007).
2 L. J. Perkins, R. Betti, K. N. LaFortune, and W. H. Williams, Phys. Rev. Lett. 103, 045004 (2009).
3 S. Atzeni, X. Ribeyre, G. Schurtz, A. J. Schmitt., B. Canaud, R. Betti, L. J. Perkins, Nuclear Fusion 54, 054008 (2014).
4 D. Batani, S. Baton, A. Casner, S. Depierreux, M. Hohenberger, O. Klimo, M. Koenig, C. Labaune, X. Ribeyre, C. Rousseaux, G. Schurtz, W. Theobald and V.T. Tikhonchuk, Nuclear Fusion 54, 054009 (2014).
5 S.Atzeni, A Schiavi and A Marocchino, Plasma Phys. Controlled Fusion 53, 035010 (2011).
6 A. Marocchino, S. Atzeni, A. Schiavi, Phis. Plasmas 21, 012701 (2014).
7 X. Ribeyre, G. Schurtz, M. Lafon, S. Galera, and S. Weber, Plasma Phys. Controlled Fusion 51, 015013 (2009).
8 A. Casner, T. Caillaud, S. Darbon, A. Duval, I. Thfouin, J.P. Jadaud, J.P. LeBreton, C. Reverdin, B. Rosse, R. Rosch, N. Blanchot, B. Villette, R. Wrobel, J.L. Miquel, High Energy Density Physics 17, 2-11 (2015).
9 E.I. Moses, R.N. Boyd, B.A. Remington, C.J. Keane, R. Al-Ayat, Phys. Plasmas 16, 041006 (2009).
10 W. Theobald, R. Nora, W. Seka, M. Lafon, K.S. Anderson, M. Hohenberger, F.J. Marshall, D.T. Michel, A.A. Solodov, C. Stoeckl, D.H. Edgell, B. Yaakobi, A. Casner, C. Reverdin, X. Ribeyre, A. Shvydky, A. Vallet, J. Peebles, F.N. Beg, M.S. Wei, R. Betti, Phys. Plasmas 22, 056310 (2015).
11 R. Nora, W. Theobald, R. Betti, F. J. Marshall, D.T. Michel, W. Seka, B. Yaakobi, M. Lafon, C. Stoeckl, J. Delettrez, A.A. Solodov, A. Casner, C. Reverdin, X. Ribeyre, A. Vallet, J. Peebles, F. N. Beg, M. S. Wei, Phys. Rev. Lett. 114, 045001 (2015).
12 L.J. Perkins, R. Betti, K.N. LaFortune, W.H. Williams, Phys. Rev. Lett. 103, 045004 (2009); R. Betti, W. Theobald, C.D. Zhou, K.S. Anderson, P.W. McKenty, S. Skupsky, D. Shvarts, V.N. Goncharov, J.A. Delettrez, P.B. Radha, J. Phys.: Conf. Ser. 112, 022024 (2008).
13 A.R. Bell and M. Tzoufras, Plasma Phys. Control. Fusion 53, 045010 (2011).

14 Ph. Nicolai, J.L. Feugeas, T. Nguyen-bui, V. Tikhonchuk, L. Antonelli, D. Batani, Y. Maheut, Phys. Plasmas 22, 042705 (2015).
15 R.K. Kirkwood, J.D. Moody, J. Kline, E. Dewald, S. Glenzer, L. Divol, P. Michel, D. Hinkel, R. Berger, E. Williams, J. Milovich, L. Yin, H. Rose, B. MacGowan, O. Landen, M. Rosen, J. Lindl, Plasma Phys. Control. Fusion 55, 103001 (2013).
16 D.S. Montgomery, J.A. Cobble, J.C. Fernández, R.J. Focia, R.P. Johnson, N. Renard-LeGalloudec, H.A. Rose, D.A. Russell, Phys. Plasmas 9, 2311 (2002).
17 S. Depierreux, J. Fuchs, C. Labaune, A. Michard, H. A. Baldis, D. Pesme, S. Hüller, G. Laval, Phys. Rev. Lett. 84, 2869 (2000).
18 L. Yin, B.J. Albright, H.A. Rose, K.J. Bowers, B. Bergen, D.S. Montgomery, J.L. Kline, J.C. Fernández, Phys. Plasmas 16, 113101 (2009).
19 L. Yin, B.J. Albright, K.J. Bowers, W. Daughton, H.A. Rose, Phys. Rev. Lett. 99, 265004 (2007).
20 L. Yin, B.J. Albright, H.A. Rose, D.S. Montgomery, J.L. Kline, R.K. Kirkwood, P. Michel, K.J. Bowers, B. Bergen, Phys. Plasmas 20, 012702 (2013).
21 R. Yan, J. Li, C. Ren, Phys. Plasmas 21, 062705 (2014).
22 M.M. Skoric, M.M. Jovanovic, M.R. Rajkovic, Phys. Rev. E53, 4056 (1996); ibid., AIP Conf. Proc. 318, 380 (1994).
23 H.X. Vu, D.F. DuBois, B. Bezzerides, Phys. Plasmas 9, 1745 (2002).
24 S. Depierreux, V. Yahia, C. Goyon, G. Loisel, P.-E. Masson-Laborde, N. Borisenko, A. Orekhov, O. Rosmej, T. Rienecker, C. Labaune, Nat. Commun. 5, 4158 (2014).
25 C. Riconda, S. Weber, V.T. Tikhonchuk, A. Héron, Phys. Plasmas 18, 092701 (2011).
26 O. Klimo, V.T Tikhonchuk, Plasma Phys. Control. Fusion 55, 095002 (2013).
27 O. Klimo, J. Psikal, V. T. Tikhonchuk, S. Weber, Plasma Phys. Control. Fusion 56, 055010 (2014).
28 A. Marocchino, M. Tzoufras, S. Atzeni, A. Schiavi, P.D. Nicolai, J. Mallet, V. Tikhonchuk, J.L. Feugeas, Phys. Plasmas 20, 022702 (2013).
29 A. Colaïtis, G. Duchateau, X. Ribeyre, Y. Maheut, G. Boutoux, L. Antonelli, Ph. Nicolaï, D. Batani, and V. Tikhonchuk, Phys. Rev. E 92, 41101 (2015).
30 A. Marocchino, S. Atzeni, and A. Schiavi, New Journal of Physics 17, 1 (2015).
31 W. Theobald, R. Nora, M. Lafon, A. Casner, X. Ribeyre, K.S. Anderson, R. Betti, J.A. Delettrez, J.A. Frenje, V.Yu. Glebov, O.V. Gotchev, M. Hohenberger, S.X. Hu, F.J. Marshall, D.D. Meyerhofer, T.C. Sangster, G. Schurtz, W. Seka, V.A. Smalyuk, C. Stoeckl, B. Yaakobi, Phys. Plasmas 19, 102706 (2012).
32 M. Hohenberger, W. Theobald, S.X. Hu, K.S. Anderson, R. Betti, T.R. Boehly, A. Casner, D.E. Fratanduono, M. Lafon, D.D. Meyerhofer, R. Nora, X. Ribeyre, T.C. Sangster, G. Schurtz, W. Seka, C. Stoeckl, B. Yaakobi, Phys. Plasmas 21, 022702 (2014).
33 C. Goyon, S. Depierreux, V. Yahia, G. Loisel, C. Baccou, C. Courvoisier, N.G. Borisenko, A. Orekhov, O. Rosmej, C. Labaune, Phys. Rev. Lett. 111, 235006 (2013).
34 S.D. Baton, M. Koenig, E. Brambrink, H.P. Schlenvoigt, C. Rousseaux, G. Debras, S. Laffite, P. Loiseau, F. Philippe, X. Rybeyre, G. Schurtz, Phys. Rev. Lett. 108, 195002 (2012).
35 S. Depierreux, P. Loiseau, D.T. Michel, V. Tassin, C. Stenz, P.E. Masson-Laborde, C. Goyon, V. Yahia, C. Labaune, Phys. Plasmas **19**, 012705 (2012).
36 A. Giulietti, A. Macchi, E. Schifano, V. Biancalana, C. Danson, D. Giulietti, L.A. Gizzi, O. Willi, Phys. Rev. E 59, 1038 (1999).
37 J. Ullschmied, Radiat. Eff. Defect S., 170, 278–289 (2015).
38 P. Koester, L. Antonelli, S. Atzeni, J. Badziak, F. Baffigi, D. Batani, C.A. Cecchetti, T. Chodukowski, F. Consoli, G. Cristoforetti, R. De Angelis, G. Folpini, L.A. Gizzi, Z. Kalinowska, E. Krousky, M. Kucharik, L. Labate, T. Levato, R. Liska, G. Malka, Y. Maheut, A. Marocchino, P. Nicolai, T. O'Dell, P. Parys, T. Pisarczyk, P. Raczka, O. Renner, Y.J. Rhee, X. Ribeyre, M. Richetta, M. Rosinski, L. Ryc, J. Skala, A. Schiavi, G. Schurtz, M. Smid, C. Spindloe, J. Ullschmied, J. Wolowski, A. Zaras5 Plasma Phys. Control. Fusion 55, 124045 (2013).
39 D. Batani, L. Antonelli, S. Atzeni, J. Badziak, F. Baffigi, T. Chodukowski, F. Consoli, G. Cristoforetti, R. De Angelis, R. Dudzak, G. Folpini, L. Giuffrida, L. A. Gizzi, Z. Kalinowska, P. Koester, E. Krousky, M. Krus, L. Labate, T. Levato, Y. Maheut, G. Malka, D. Margarone, A. Marocchino, J. Nejdl, Ph. Nicolai, T. O'Dell, T. Pisarczyk, O. Renner, Y. J. Rhee, X. Ribeyre, M. Richetta, M. Rosinski, M. Sawicka, A. Schiavi, J. Skala, M. Smid, Ch. Spindloe, J. Ullschmied, A. Velyhan, T. Vinci, Phys. Plasmas 21, 032710 (2014).
40 T. Pisarczyk, S.Yu. Gus'kov, Z. Kalinowska, J. Badziak, D. Batani, L. Antonelli, G. Folpini, Y. Maheut, F. Baffigi, S. Borodziuk, T. Chodukowski, G. Cristoforetti, N. N. Demchenko, L. A. Gizzi, A. Kasperczuk, P. Koester, E. Krousky, L. Labate, P. Parys, M. Pfeifer, O. Renner, M. Smid, M. Rosinski, J. Skala, R. Dudzak, J. Ullschmied, P. Pisarczyk, Phys. Plasmas 21, 012708 (2014).
41 J. Badziak, L. Antonelli, F. Baffigi, D. Batani, T. Chodukowsi, G. Cristoforetti, R. Dudzak, L.A. Gizzi, G. Folpini, F. Hall, Z. Kalinowska, P. Koester, E. Krousky, M. Kucharik, L. Labate, R. Liska, G. Malka, Y.

Maheut, P. Parys, M. Pfeifer, T. Pysarczyk, O. Renner, M. Rosinski, L. Ryc, J. Skala, M. Smid, C. Spindloe, J. Ullschmied, A. Zaras-Szydlowska, Laser Part. Beams 33, 561 (2015).
42 L. Antonelli, P. Koester, G. Folpini, Y. Maheut, F. Baffigi, G. Cristoforetti, L. Labate, T. Levato, L.A. Gizzi, F. Consoli, R. De Angelis, Z. Kalinowska, T. Chodukowski, M. Rosinski, P. Parys, T. Pisarczyk, P. Raczka, L. Ryc, J. Badziak, J. Wolowski, M. Smid, O. Renner, E. Krousky, M. Pfeifer, J. Skala, J. Ullschmied, P. Nicolai, X. Ribeyre, G. Shurtz, S. Atzeni, A. Marocchino, A. Schiavi, C. Spindloe, T. O'Dell, Y. J Rhee, M. Richetta, D. Batani, Journal of Physics: Conference Series 688, 012003 (2016).
43 L. Labate, T. Levato, M. Galimberti, A. Giulietti, D. Giulietti, M. Sanna, C. Traino, M. Lazzeri, L.A. Gizzi, Nucl. Instrum. Meth. Phys. Res. A 594, 278-282 (2008)
44 C.D. Chen, J.A. King, M.H. Key, K.U. Akli, F.N. Beg, H. Chen, R.R. Freeman, A. Link, A.J. Mackinnon, A.G. MacPhee, P.K. Patel, M.Porkolab, R.B. Stephens, and L.D. Van Woerkom, Rev. Sci. Instr. 79, 10E305 (2008).
45 S. Atzeni, A. Schiavi, F. Califano, F. Cattani, F. Cornolti, D. Del Sarto, T. Liseykina, A. Macchi, F. Pegoraro, Computer Phys. Commun., 169, 153-159 (2005); S. Atzeni, Computer Phys. Commun., 43**,** 107-124, (1986).
46 J. Breil, S. Galera, and P. H. Maire, Comput. Fluids 46, 161 (2011).
47 J.J. MacFarlane, I.E. Golovkin, P. Wang, P.R. Woodruff, N.A. Pereyra, High Energy Density Physics 3, 181 (2007).
48 J. Myatt, A. V. Maximov, W. Seka, R. S. Craxton, and R. W. Short, Phys. Plasmas, 11, 3394, (2004).
49 W. L. Kruer, in The Physics of Laser Plasma Interactions, Frontiers in Physics, Vol. 73, edited by D. Pines Addison–Wesley, Redwood City, CA, 1988.
~~4508~~ R.E. Turner, D.W. Phillion, B.F. Lasinski, E.M. Campbell, Phys. Fluids 27, 511 (1984).
~~5149~~ W. Seka, B.B. Afeyan, R. Boni, L.M. Goldman, R.W. Short, K. Tanaka, T.W. Johnston, Phys. Fluids 28, 2570 (1985).
~~520~~ W. Seka, D.H. Edgell, J.F. Myatt, A.V. Maximov, R.W. Short, V.N. Goncharov, H.A. Baldis, Phys. Plasmas 16, 052701 (2009).
~~531~~ B.B. Afeyan, E.A. Williams, Phys. Rev. Lett. 75, 4218 (1995).
~~542~~ R.L. Berger, L.V. Powers, Phys. Fluids, 28, 2895 (1985).
55 R. Yan, A.V. Maximov, C. Ren, Phys. Plasmas 17, 052701 (2010).
56 W. Seka, J.F. Myatt, R.W. Short, D.H. Froula, J. Katz, V.N. Goncharov, I.V. Igumenshchev, Phys. Rev. Lett. 112, 145001 (2014).
57 C.Z. Xiao, Z.J. Liu, C.Y. Zheng, X.T. He, Phys. Plasmas 23, 022704 (2016).
58 R. Yan, C. Ren, J. Li, AV. Maximov, W.B. Mori, Z.-M. Sheng, F.S. Tsung, Phys. Rev. Lett. 108, 175002 (2012).
59 D. A. Russell and D. F. DuBois, Phys. Rev. Lett. 86, 428 (2001).
~~6053~~ S. Weber, C. Riconda, High Power Laser Science and Engineering, 3 doi:10.1017/hpl.2014.50 (2015).
~~6154~~ D. Batani, C. Bleu, and Th. Lower, Eur. Phys. J. D 19, 231–243 (2002).
~~6255~~ M.N. Rosenbluth, Phys. Rev. Lett. 29, 565 (1972).
~~6356~~ C.S. Liu, M.N. Rosenbluth, R.B. White, Phys. Fluids 17, 1211 (1974).
64 H.X. Vu, D.F. DuBois, B. Bezzerides, Phys. Plasmas 14, 012702 (2007).
~~57 D.W. Forslund, J.M. Kindel, L. Lindman, Phys. Fluids 18,1002 (1975).~~
~~6558~~ G. Cristoforetti, A. Colaïtis, L. Antonelli, S. Atzeni, F. Baffigi, D. Batani, F. Barbato, G. Boutoux, R. Dudzak,P. Koester, E. Krousky, L. Labate, Ph. Nicolai, O. Renner, M. Skoric, V. Tikhonchuk, L.A. Gizzi, EPL 117, 35001 (2017).
~~6659~~ L. Yin, B.J. Albright, K.J. Bowers, W. Daughton, H.A. Rose, Phys. Plasmas 15, 013109 (2008).
~~6760~~ S. Miyamoto, K. Mima, M.M. Škorić, M.S. Jovanović, J. Phys. Soc. Japan 67, 1281 (1998).
68 C. Riconda and S. Weber, High Power Laser Science and Engineering, 4, e23 (2016).
69 G.J. Morales, T.M. O'Neal, Phys. Rev. Lett. 28, 417 (1972).
70 R.L. Dewar, Phys. Fluids 15, 712 (1972).
71 K. Estabrook, W. Kruer, Phys. Fluids 26, 1892 (1983).
72 T. Kolber, W. Rozmus, V.T. Tikhonchuk, Phys. Fluids B 5, 138 (1993).
73 M.M. Skoric, J. Plasma Phys. 79, 1003 (2013); ibid., J. Phys.: Conf. Ser. 688, 012112 (2016).
74 T. Chapman, S. Huller, P.E. Masson-Laborde, A. Heron, D. Pesme, W. Rozmus, Phys. Rev. Lett. 108, 145003 (2012).
~~61 K. Estabrook, W. Kruer, Phys. Fluids 26, 1892 (1983).~~
~~62 T. Kolber, W. Rozmus, V.T. Tikhonchuk, Phys. Fluids B 5, 138 (1993).~~
~~63 G.J. Morales, T.M. O'Neal, Phys. Rev. Lett. 28, 417 (1972).~~
~~64 R.L. Dewar, Phys. Fluids 15, 712 (1972).~~
~~65 M.M. Skoric, J. Plasma Phys. 79, 1003 (2013); ibid., J. Phys.: Conf. Ser. 688, 012112 (2016).~~75 Estar database: http://physics.nist.gov/PhysRefData/Star/Text/ESTAR.html
~~7666~~ J. Sempau, E. Acosta, J. Barò, J.M. Fernandez-Varea, F. Salvat, Nuclear Inst. Method B, 132, 377 (1997).

77~~67~~ S. Agostinelli, J. Allison, K. Amako , J. Apostolakis, H. Araujo, P. Arcel, M. Asaig, D. Axen, S. Banerjee, G. Barrand, et al., Nuclear Inst. Method A, 506, 250 (2003).

78 S. Von Goeler, J. Stevens, S. Bernabei, M. Bitter, T.K. Chu, P. Efthimion, N. Fisch, W. Hooke, K. Hill, J. Hosea, F. Jobes, C. Karney, J. Mervine, E. Meservey, R. Motley, P. Roney, S. Sesnic, K. Silber, G. Taylor, Nuclear Fusion, 25, No. 11 (1985).~~68 Estar database: http://physics.nist.gov/PhysRefData/Star/Text/ESTAR.html~~